In situ X-ray tomography characterisation of 3D deformation of C/C-SiC composites loaded under tension

Yang Chen, Yuan Shi, Camille Chateau, James Marrow

In situ X-ray tomography characterisation of 3D deformation of C/C-SiC composites loaded under tension

Yang Chen [a], Yuan Shi [b, #], Camille Chateau [c], James Marrow [a]

[a] Department of materials, University of Oxford, Parks Road, OX1 3PH, Oxford, UK

[b] Institute of Structures and Design, German Aerospace Center (DLR) Stuttgart, Pfaffenwaldring 38-40, 70569 Stuttgart, Germany

[c] Laboratoire Navier, Ecole des Ponts ParisTech, Univ Gustave Eiffel, CNRS, 77455 Marne-la-Vallée, France

[#] Corresponding author: Yuan. Shi (yuan.shi@dlr.de)

Abstract

C/C-SiC composites fabricated through Liquid Silicon Infiltration were tested under monotonic tension with in situ X-ray computed tomography. The specimens had different fibre orientations with respect to the tensile direction, 0º/90º and ±45º, such that the tension accounted for in-axis and off-axis loads, respectively. The 3D XCT images provided explicit visualisations and quantitative measurements of the distributions of SiC-Si and the orientations of the C fibre bundles. The full-field displacement and strain fields were measured by Digital Volume Correlation, observing a difference in the local deformations in response to the in-axis and off-axis loading. In both specimens, the tensile load triggered significant strain localisations at low stress (<50 MPa). Strong local deformations, observed at both low and high applied stresses, were mostly in the through-thickness direction, indicating local delamination. These observations show the importance of residual stresses to damage development in C/C-SiC composites.

Keywords

A. Ceramic-matrix composites (CMCs); B. Mechanical properties; C. Micro-mechanics; D. CT analysis

1. Introduction

Because of its favourable fracture toughness, comparatively low density and resistance against severe environments (temperature, corrosive atmospheres, etc.), carbon fibre reinforced silicon carbide (C/C-SiC), such as developed via Liquid Silicon Infiltration (LSI) at the Institute of Structures and Design of German Aerospace Centre (DLR), has potential applications in areas including aerospace, traffic and energy technology [1–5]. Some macroscopic mechanical properties of C/C-SiC material have been studied previously, including the tensile and bending strength in varying loading directions [6] and the damage mechanisms with different fibre architectures through a modal acoustic emission (AE) technique [7]. Different statistical distributions of strength under different loading states have been observed [8] and the effects of temperatures on the mechanical properties have been investigated [9]. However, the effect of different fibre orientations and thermal residual stresses on the localisation and orientation of local strain is still not understood in detail.

As a non-destructive approach, X-ray computed tomography (XCT) is particularly attractive and has been successfully used to characterise a range of ceramic matrix composites, see e.g. [10–15]. XCT provides direct 3D information of the internal material structures, typically at micrometre resolution. It also offers the possibility to monitor the microstructural evolution in response to mechanical loading through in situ testing. Both qualitative observations and quantitative measurements can be obtained from XCT images, from which the Digital volume correlation (DVC) technique is the most common tool to measure the full-field displacements and then the localised strain fields of the microstructure [16]. DVC-measured strain maps can be used as a faithful indicator of local damage, see [17–19] among others. DVC-assisted image subtraction or DVC residuals also allows the 3D complex crack networks to be detected [14,18,20]. Moreover, quantitative measurements of the crack networks in CMCs can also be extracted using advanced image processing algorithms, see e.g. [21].

In the present work, in situ XCT tensile tests have been conducted with monotonic loading on two specimens with different fibre orientations 0º/90º and ±45º, such that the tension could account for in-axis and off-axis loads. The 3D local deformations have been measured by DVC. The strain localisations are analysed in detail in relation with fibre architectures. The important contribution of residual stresses is discussed according to the observed strain localisations within the woven structures.

2. Materials and Method

The investigated C/C-SiC material was produced by a three-stage process. First, CFRP (Carbon Fibre Reinforced Polymer) preforms with fibre orientations of 0°/90° were manufactured via warm pressing at around 200 °C using prepregs based on phenolic resin precursor and a stack of 2D carbon fibre fabrics (3K HTA fibres of Teijin Carbon Europe GmbH). Then in a subsequent carbonization stage, the green body (fibre fabrics) was pyrolyzed at about 1600 °C in nitrogen atmosphere and the phenolic resin matrix was converted into carbon. Finally, liquid silicon was infiltrated into the porous C_f/C_m body at above 1600 °C to form SiC by reaction. The more detailed description of the three-stage process for C/C/SiC fabrication has been summarized in [9]. The material phase compositions of the final C/C-SiC composite are: 80~85 vol. % of C (C fibres and amorphous C matrix), 10~15 vol. % of SiC and 1~5 vol. % of residual Si. The fibre volume content, porosity and density are approx. 60 %, 2 % and 2.0 g/cm³, respectively. The fibre volume content of the samples was determined through the measurement of the initial weight of the fibres and the total weight of the component. The porosity of the specimens was measured using the Archimedes method [22]. Two dog-bone shaped coupons were cut from the same C/C-SiC composite plate through water jet technology. Different cutting directions were used to produce the two specimens with different fibre orientations with respect to the loading direction. Hereafter, the specimen with 0º/90º and ±45º fibre orientations will be referred to as 0/90 specimen and ±45 specimen, respectively.

Figure 1 shows the experimental setup for the in-situ tests. The specimen was loaded with a Deben CT5000 loading rig (5 kN load cell). The fixation of the specimen was enhanced with steel pins passing through the holes on the top and bottom tabs of the dog-bone coupon. XCT scans were performed using an Xradia Versa 510 microscope at different loading steps. The same scan parameters were applied to the scans of both 0/90 and ±45 specimens. The X-ray beams were generated with 60 kV electron energy and 5 W power. Each scan consisted of 1601 projections over a 360º rotation, each with an exposure time of 35 s, leading to a scan time of about 15 h. 3D images were then reconstructed with voxel size of 5.8 µm and dimensions of 11.6 × 11.8 × 11.7 mm. They were converted into 8-bit integer format. After a reference scan at the unloaded state, the 0/90 and ±45 specimens were scanned at four and three successive loading steps, respectively. Table 1 shows the applied tensile stresses for each step. The tensile load was applied by displacement-controlled cross-head moving with a speed of 0.1 mm/min. The displacement was kept constant during the scans.

A cross-sectional slice of the 0/90 specimen at the reference step is shown in Figure 2. The section is perpendicular to the tensile loading direction. In the reconstructed XCT image, the regions of SiC and Si (bright voxels, higher attenuation) cannot be faithfully separated from each other due to the similar attenuations and to the small quantity of Si, yet they can be clearly distinguished from other regions (dark voxels, lower attenuation). In the dark regions (see the zoomed-in view of Figure 2), transverse cracks can also be observed in addition to pores inside the C_f/C_m blocks. As will be discussed later in Section 4.1, these transverse cracks were probably produced by thermal strains from the higher coefficient of thermal expansion (CTE) of the carbon fibres in the radial direction, relative to the SiC matrix.

3. Data processing

3.1 Image segmentation

To obtain a quantitative assessment of the main features of the composite structure, the 8-bit greyscale images were segmented using a supervised clustering technique [23]. In our implementation (MATLAB[1] scripts), the spatial resolution of the initial XCT image (5.8 µm/voxel) was kept in the segmentation result. A structure tensor is first calculated at each voxel with a 5-point centred differentiation of the voxel grey scale over a subvolume. This subvolume should be large enough to minimize the effect of noise and small enough to make the calculated structure tensor sensitive to local information. In the present case, a cube of 7×7×7 voxels (larger than fibre diameter and smaller than fibre bundle dimension) was chosen, which provided optimal segmentation results according to some preliminary tests. The eigenvector corresponding to the minimum eigenvalue of the structure tensor indicates the local fibre orientation. Also, the ratio between the minimum and maximum eigenvalues ($\beta = \lambda_{min}/\lambda_{max}$) measures the local anisotropy, e.g. a value of β close to zero suggests a strong preferential orientation of the considered voxel, indicating a voxel located within a fibre bundle; on the contrary, a value of β close to one indicates a voxel located within the matrix or a void. Together with the grey level, these measurements of orientation and anisotropy are used to construct a vector of feature parameters for each voxel. Finally, a supervised clustering is conducted with a Gaussian-type mixture model. This

[1] https://ch.mathworks.com/products/matlab.html

compares the feature parameters of each voxel to those of training sets. In the present work, the training sets (one per cluster) were manually selected from the same XCT image under investigation, representing the regions outside the specimen (void voxels) and the fibre bundles with different orientations. The SiC-Si voxels, which could be assigned also to the two groups of fibre bundles (with different fibre orientations), were distinguished by their grey levels.

The greyscale contrast between SiC and Si, due to their similar X-ray attenuation coefficients, is not sufficient for them to be separated by image processing. Furthermore, due to the limited spatial resolution of the XCT images, as well as their random noise, it was not possible to faithfully separate all the pores and cracks in the C_f/C_m. Therefore, only some typical pores and thermal cracks were manually segmented from the XCT images to provide a qualitative illustration (Section 4.1).

3.2 Strain measurement

The microstructural heterogeneity observed in the greyscale XCT images provides the contrast markers for DVC calculations. 3D local displacement fields and strain fields were obtained using the DaVis[2] software (version 8.4.0). Each DVC analysis was conducted with first an FFT correlation, then followed by four steps of direct correlations with decreasing cubic correlation windows (i.e. subsets) with dimensions of 128 voxels, 64 voxels, 32 voxel and 16 voxels per side. A structured correlation grid was used in these successive correlations, with an 8 voxel spacing between correlation points at the final correlation step. 3D local strain fields were then calculated from the DVC-measured displacement fields with 3-point centred differentiation. The same parameters were used to process the images at all loading steps of both specimens. The 3D strain fields will be analysed in combination with the microstructures and some 3D visualisations (obtained using either Avizo Fire[3] (version 2020.01), or Paraview[4]) will be shown in the next section.

Incremental DVC analysis was done (i.e. between successive loading steps), instead of the classical analysis that considers each loading step relative to the unloaded reference step. This is because of the observation, reported in Section 4.2.1, that the strain localisations induced by the first loading step are much stronger than those induced by the later increments. In Table 2, *Load-A* refers to the increment

[2] https://www.lavision.de/en/products/strainmaster/dvc/
[3] https://www.thermofisher.com/uk/en/home.html
[4] https://www.paraview.org/

between the reference (i.e. unloaded, 'Ref.') step and the first loading step, while *Load-B* is the increment between the reference and the final loading step of the in situ test. *Load-AB* refers to the increment between the first loading step and the final loading step. The other sequential load increments, which will be called as "*late loading increments*", are denoted by *Load-ij*, with i,j indicating the loading steps that were correlated in the DVC calculation. These notations will be used in the later discussions in Section 4.

4. Results and discussions

First, the microstructures of the as-received materials will be analysed from the image segmentation results, followed by a discussion on the formation mechanisms of thermal cracks and residual stresses. Then, the local 3D deformations will be characterised with the DVC results, demonstrating the importance of residual stresses on the development of strain localisations within the C/C-SiC composites.

4.1 Analysis of initial microstructure

4.1.1 Observation from XCT images

The results of image segmentation are shown in Figure 3 for both specimens. These 3D visualisations suggest that the SiC-Si forms wall-like structures separating each fibre bundle into several C_f/C_m blocks. In addition, the SiC-Si regions are mostly interconnected within the adjacent fibre bundles of different orientations, leading to a large interconnected network within the whole composite. This geometric structure of the SiC-Si is a direct consequence of the LSI process, in which the liquid Si reacting with the carbon matrix to form SiC penetrates into intra-bundle pores and thermal cracks (from the prior pyrolysis process), via the connected inter-bundle pores.

Since the two specimens were cut from the same C/C-SiC composite plate, we choose to analyse the microstructure of the 0/90 specimen only. Figure 4 illustrates the 3D geometries of some (not all) intra-bundle pores and a thermal crack within a small subvolume at the reference step (unloaded). The pores and the crack have been manually identified using the "magic wand" option in Avizo (a seed growing image segmentation algorithm). The large thermal crack is interconnected and has an overall dimension of several millimetres. Similar to the thermal cracks, the intra-bundle pores have geometries aligned with the adjacent fibre orientation, though their dimensions are much smaller than that of the crack.

Overlaying the crack onto the SiC-Si regions in Figure 4.b, we observe that the thermal crack in a 0º bundle is mainly parallel to the neighbouring 0º SiC-Si regions and it has been formed by the connection of several thermal cracks within different 0º bundles. Note that similar thermal cracks and inter-bundle pores have also been observed in 90º bundles, which are not shown here for the sake of conciseness.

4.1.2 Possible mechanisms of thermal crack formation

Thermal cracks in such composites can be produced by cooling shrinkage during the manufacturing. Combining the observations in Figures 2-4, we propose the following mechanisms by which the microstructure accommodates shrinkage, which is similar as those proposed by [24]. The coefficients of thermal expansion (CTE) of the constitutive materials have been reported in [24] and the references therein. SiC and Si have similar isotropic CTE of $4.1 \times 10^{-6}\ K^{-1}$ and $4.6 \times 10^{-6}\ K^{-1}$, respectively, whereas the CTE of C fibres differs significantly between the radial direction ($13 \times 10^{-6}\ K^{-1}$) and the axial direction ($1 \times 10^{-6}\ K^{-1}$). The CTE of the amorphous carbon matrix of the present material was not found in the literature, though [25] have reported an interval of CTE between $1.5 \times 10^{-6}\ K^{-1}$ and $3.8 \times 10^{-6}\ K^{-1}$ for hydrogenated amorphous carbon. Due to these CTE mismatches, complex 3D patterns of residual stress will be generated during the manufacturing.

- First, during the cooling of the pyrolysis process, C fibres exhibit more shrinkage in their radial direction than the surrounding carbon matrix. The bonding between fibres and matrix is assumed relatively strong, so that radial tensile thermal stresses produce intra-bundle matrix cracks parallel to the fibres (forming a network of transverse cracks in the plane of the composite) and inter-bundle delamination in the through-thickness direction. The complex (mainly shear) residual stresses at the boundaries of fibre bundles could also contribute to the inter-bundle delamination. Note that initial shrinkage might also have occurred prior to the cooling down, when the phenolic resin was converted to carbon at high temperature.
- These cracks in the C_f/C_m structure would be mostly penetrated and filled up by liquid silicon during the LSI process. Therefore, the cracks observed in the XCT images should be mainly from the LSI process. During the cooling phase of the LSI process, the C fibres again shrink more than the surrounding matrix in the radial direction, resulting in new thermal cracks that are similar to those from the cooling of pyrolysis process.

Residual stresses could be mainly created during the LSI cooling process. The lower CTE of C fibres in the axial direction will cause the fibres to be compressed axially, with the matrix (both SiC-Si and C) experiencing tension in the axial direction of each fibre bundle. The boundaries between fibre bundles will carry complex residual stresses due to the varying orientations of fibres. These residual stresses will be discussed to interpret the strain localisations in Section 4.2.3.

4.2 3D deformation field

Incremental macroscopic strains along the three coordinate axes were first measured for each load increment from the DVC results. This was done using the net displacement change over a virtual gauge between two sets of the correlation points located at two opposite layers of the correlation grid along the Y-axis, X-axis and Z-axis, with gauge lengths of ~4.6mm, ~4.6 mm and ~1.6 mm, respectively. Then, cumulative macroscopic strains relative to the reference step are obtained by summing up these incremental strain values. The results are given in Figure 5 as a function of the applied macroscopic stresses. The stress-strain curves from some continuous tests by [9,26] on composites manufactured using the same or similar method, with larger specimen dimensions, are also provided for comparison. The 0/90 specimens exhibit a good reproducibility of the stress-strain behaviour between different tests. However, a clear difference is observed for the ±45 specimens, which could be due to the off-axis behaviour of the composite being more sensitive to specimen dimensions [27]. The boundary conditions of the central gauge region of each specimen has been verified (Supplementary material 5), showing that the flexion due to slight misalignment is not detrimental and the major loading mode remains tension.

Comparing the loading-axis response (E_{yy}) of both specimens, the ±45 specimen exhibits higher strain-to-failure and a lower strength than the 0/90 specimen, which is a common behaviour of woven CMCs [14,26,28]. For the 0/90 specimen, both the transverse strain E_{xx} and the through-thickness strain E_{zz} remain close to zero. For the ±45 specimen, the transverse strain E_{xx} is negative with increasing absolute value as the tensile load increases, while its through-thickness strain E_{zz} has increasing positive values. This positive E_{zz} of the ±45 specimen, indicating a negative Poisson's ratio, is the macroscopic consequence of local delamination-like deformations (see later in Section 4.2.3). A similar observation has also been reported by [14] for SiC/SiC composite tubes.

These macroscopic behaviours will be discussed together with the local deformations, which will be analysed in detail in the next sections. We will start with the high-magnitude strains (definition in Section 4.2.1) as they are usually considered as indicators of local damage that contributes to failure. Then, the low-magnitude strains will be analysed in Section 4.2.4. In the following, maps of maximum principal strains will be presented for the whole scanned regions. The statistical analyses, such as the probability density functions and the densities of orientations, are calculated only for the central gauge region (with minimum uniform section) of each dog-bone specimen.

4.2.1 Depletion of "weak points"

Figure 6 compares the localised strains created by different loading increments: *Load-A*, *Load-B* and *Load-AB,* presented as maximum principal strain magnitude. For both specimens, the most significant strain localisations have been induced by *Load-A* only, with magnitude up to 0.03; while *Load-AB* induces only low-magnitude (<0.005) strains with a more uniform distribution within the microstructure. Correlation of late stage observations with the reference (i.e. *Load-B*) does not reveal this development because the smaller magnitude strains that develop at higher stress cannot be seen against the background of the higher magnitude strains that developed initially. This phenomenon can be observed in both the 0/90 and ±45 specimens. It shows that the localised deformation in the C/C-SiC composites exhibits a non-uniform development with respect to the mechanical load, i.e. the most significant strain localisations occur at a small load. This may be due to the triggering of pre-existing "weak-points". The term "weak point" used herein refers to a zone whose deformation is quite sensitive to external load. After the opening of these weak points at low stress, the development of localised strains at higher stress is more uniformly distributed throughout the heterogeneous microstructure (Figure 6). This suggests that most of the weak points have been depleted during the first loading step (i.e. *Load-A*). Some possible origins of these weak points will be discussed in a remark at the end of Section 4.2.2.

The above qualitative trends shown in Figure 6 are confirmed by examination of the statistical distributions of strains produced by each sequential load increment. The probability density functions of maximum principal strains ε_{max} are shown in Figure 7. For both specimens, a much wider range of ε_{max} with a significantly higher mode value is induced by the first increment (*Load-A*) than by the late increments (*Load-ij*). The late loading increments produced narrower statistical distributions of ε_{max} with

a smaller mode than that of the first loading increment. The distributions of ε_{max} are quite similar in the late loading increments with a mode of $\varepsilon_{max}{\sim}0.002$ for both specimens.

In the following, the strain data will be classified into two groups according to their maximum principal values ε_{max}. The thresholding values ε^{thr} are indicated on the probability functions shown in Figure 7. For the 0/90 specimen, we choose $\varepsilon^{thr} = 0.022$ for *Load-A* and $\varepsilon^{thr} = 0.007$ for *Load-ij*; for the ±45 specimen, we choose $\varepsilon^{thr} = 0.012$ for *Load-A* and $\varepsilon^{thr} = 0.006$ for *Load-ij*. Strains with $\varepsilon_{max} < \varepsilon^{thr}$ will be referred to as "low-magnitude strains" and those with $\varepsilon_{max} \geq \varepsilon^{thr}$ as "high-magnitude strains". These arbitrary values of ε^{thr} were chosen to correspond to approximately 90% (±5%) of the cumulative distributions for both specimens at different loading increments.

4.2.2 Location and orientation of high-magnitude strains ($\varepsilon_{max} > \varepsilon^{thr}$) at low applied load

To examine the locations and the principal deformation directions of the high magnitude ($\varepsilon_{max} > \varepsilon^{thr}$) strain localisations that have been identified as "weak points" in cross-sectional slices of the principal strains are shown in Figure 8 for *Load-A* of each specimen. The high strain values are mostly located inside fibre bundles for both specimens, though they seem closer to the boundaries of fibre bundles for the +/-45 specimen. We recall that at least one thermal crack has been observed in each C_f/C_m block isolated by the SiC-Si walls (see Figure 2), whereas, high-magnitude strains are not found within every C_f/C_m block. This indicates that there is no systematic correlation between the thermal cracks and these strain localisations.

The principal orientations of the high-magnitude strains are shown in Figure 9.a and b. The principal vectors are tensile and mostly along the through-thickness direction, which indicate delamination-like deformation. To obtain a statistical representation of the principal orientations of the strains, their densities of orientations are calculated using the MTEX toolbox[5] and are expressed in stereographic projection as shown in Figure 9.c and d. The 2D projection coordinate system and the corresponding 3D spherical coordinate system used in the present study are defined in Appendix A. The two specimens exhibit similar distributions of the densities of orientations, confirming the 3D visualisation of Figure 9.a and b, i.e. most of the high-magnitude strains are along the through-thickness (stacking) direction.

[5] https://mtex-toolbox.github.io/Documentation.html

4.2.3 Discussion on the origins of weak points

As mentioned in Section 4.2.1, the high-magnitude strains at low applied load are believed to be related to some weak points. Here, we discuss two possible origins of the weak points: (i) some zones experiencing high residual tensile stresses, or close to pre-existing stress concentrating defects that can easily initiate local fractures; (ii) some already fractured zones whose local deformation is relatively free, requiring very small stresses to open further. We refer to the two above zones as *easy-to-break* and *free-to-deform* zones, respectively. However, it is not clear which one of them accounts for the weak points, or whether they co-exist. According to the acoustic-emission (AE) study of [26] on similar composites of larger dimensions (60 × 10 × 3 mm, dog-bone shaped), no significant AE events were detected over the macroscopic strain range of 0~0.032% for both 0/90 and ±45 specimens. Therefore, the two following scenarios are possible: (i) the *easy-to-break zones* fractured and created "quiet" (low-energy) AE events, due to the quite local residual stresses and the corresponding small strain energy; (ii) the *free-to-deform* zones, whose deformation does not release elastic energy, were in an unstable state at the beginning hence very sensitive to even a very small external load and then became stable after they opened to a certain extent. This "stabilisation" scenario implies the occurrence of some microstructural rearrangement that blocks the free-to-deform zones from continued deforming as the load increases. A possible free-to-deform zone might be closed micro-cracks, created during manufacture, cutting or sample mounting. Further investigations are necessary to make this clear.

4.2.4 High-magnitude strains ($\varepsilon_{max} > \varepsilon^{thr}$) induced by high applied load

The cross-sectional slices given in Figure 10 for the two specimens show the localised high-magnitude strains ($\varepsilon_{max} > \varepsilon^{thr}$) in each woven structure at the last loading increment (*Load-34* for the 0/90 specimen and *Load-23* for the ±45 specimen). Observing from a mesoscopic viewpoint, the distribution of strain localisations exhibits a clear correlation with the woven structure. Comparing the two specimens at microscopic scale, the high-magnitude strains occur inside the C_f/C_m blocks in the 0/90 specimens and around SiC-Si walls (including the boundaries between +45º and -45º fibre bundles) in the ±45 specimen. Furthermore, similarly as the strain localisations induced by *Load-A*, the high-magnitude strains induced by the late increment *Load-34* have no systematic correlation with the thermal cracks that were found within each C_f/C_m block. This latter is also confirmed by the crack detection result presented in Appendix B. Note that similar slices for the intermediate loading increments,

from which the same conclusions can be drawn, are included as Supplementary Materials for the sake of conciseness.

The densities of principal orientations are then shown in Figure 11 for the high-magnitude strains. The variations of the principal orientations in the 0/90 specimen are mostly in the XY plane ($\phi = \pm 90°$) with high-density populations around the Y-axis (loading direction) and the orthogonal X-axis (in the specimen plane). In comparison, the denser populations in the ±45 specimen are more pronounced in the YZ plane. In other words, for the last load increment (*Load-34* or *Load-23*), the ±45 specimen exhibits stronger delamination-like deformation than the 0/90 specimen. Similar graphs for the intermediate loading increments are shown in Supplementary Materials for the sake of conciseness, as the same conclusions can be drawn.

To sum up, both the locations and orientations of the high-magnitude strains exhibit clear differences between the two specimens. This indicates that the loading direction with respect to the fibre architecture (in-axis or off-axis) has a strong effect on the local deformations that develop during the late loading increments at higher strains, after the depletion of weak points.

To examine for an effect of the fibre orientations on the local high-magnitude strains, the densities of principal orientations measured in different fibre bundles are given in Figure 12. Obvious differences can be observed between the 0º and 90º bundles and between the +45º and -45º bundles. In the 0/90 specimen, the high-magnitude local deformations in the 0º bundles are mostly along the loading axis (Y-axis); whereas, in the 90º bundles, the majority of the local strain orientations are around the X-axis, with a smaller population along the Y-axis. This will be discussed in the next paragraph with respect to residual stresses. In the ±45 specimen, the orientation populations of either +45º or -45º bundles have some bias towards the fibre orientation, which is schematically illustrated by the right-hand side graph in Figure 12.b. In addition, a strong peak of the principal deformation orientation in the through-thickness direction is observed in both the +45º and -45º bundles.

Figure 12.a indicates that high-magnitude strains are mostly oriented along the fibre axis, even in the 90° bundles which are loaded transversally. We propose an explanation for this observation. Figure 13.a shows the principal vectors of the high-magnitude strains that developed in the last loading increment of the 0/90 specimen. We distinguish two types of strains according to their orientations: axial strains that are mainly oriented along the loading axis (Y-axis, i.e. parallel to the 0° fibres) and

transverse strains that are mainly oriented along the 90º fibres (X-axis). As highlighted by the red circles in Figure 13.a, inside 90º bundles the axial strains are located mostly at or close to SiC-Si regions, while the transverse strains are inside C_f/C_m blocks. As detailed in Section 4.1, initially the fibres are under compression and the matrix (both SiC-Si and C) under tension because of CTE mismatch. The axial tensile strains could be an indicator of local debonding between C_f/C_m blocks and SiC-Si walls. This debonding fracture is further confirmed by the crack detection result presented in Appendix B. Such local debonding could relax the local compressive residual stress in fibres within the neighbouring C_f/C_m block, thus producing transverse tensile strains along the fibre direction. In the 0º bundles, some strains perpendicular to the loading direction are also observed (see the purple arrows circled in Figure 13.a). Again, these perpendicular tensile strains occur close to SiC-C walls, indicating that debonding also occurs between SiC-Si and C in the 0º bundles. Therefore, the release of axial tensile residual stresses would contribute to the tensile strains of the adjacent C_f/C_m, in addition to the in-axis tensile load.

The scenario described above also explains the distributions of principal strain orientations in the ±45 specimen. As shown in Figure 13.b, the majority of local strains are inclined to the adjacent fibre directions for either +45º or -45º bundles (corresponding to the populations indicated by the red dots in the stereographic maps of Figure 12.b). This fibre-oriented local deformation might be a consequence of the release of the local residual stresses along the fibre directions. Moreover, some local deformations are inclined to the transverse direction of fibre bundles (circled in Figure 13.b). This orientation, corresponding to the yellow dots in the stereographic maps of Figure 12.b, could be related to the opening of debonding between SiC-Si and C_f/C_m. Due to the shear stresses induced by the off-axis load, the local strain orientations in the ±45 specimen are more complex than those in the 0/90 specimen, leading to strain orientations in the through-thickness direction.

To provide a global indication of the distribution of strain localisations in the fibre bundles with different orientations, we have counted the proportion of high-magnitude strains (DVC data points) in the total number of DVC data points in each group of fibre bundles and calculated the ratio between them (0º versus 90º, +45º versus -45º). The results are plotted in Figure 14 as a function of the macroscopic strains for each specimen at each loading increment. Starting from approximately one at the first loading increment, the ratio for the 0/90 specimen decreases, which indicates that more and more high-magnitude strains take place in 90º bundles with increasing applied strain. In contrast, the ratio for the

±45 specimen seems to fluctuate around one, which is consistent with the symmetry of +45º and -45º bundles with respect to the loading axis.

4.2.5 Densities of principal orientations for the low-magnitude strains ($\varepsilon_{max} < \varepsilon^{thr}$)

Figure 15 compares the orientations of low-magnitude strains observed in the two specimens. Both the 0/90 and ±45 specimens exhibit a concentration of orientations along the loading axis. Note that these low-magnitude strains account for the majority of the DVC measurements within each specimen. In other words, although the orientations of the high-magnitude strains are strongly affected by the composite microstructure and residual stresses, the majority of the local strains (low-magnitude) are mostly driven by the applied load. Furthermore, a band of lower density in the YZ plane is also observed in the ±45 specimen, whereas more uniform fluctuations are found in the 0/90 specimen. This could be due to the fact that shear stresses, promoting either inter-bundle or intra-bundle delamination, are more pronounced in the ±45 specimen than in the 0/90 specimen.

4.2.6 Discussion on the relationship between micro and macro strains

In Figure 5, the macroscopic transverse strain E_{xx} of the 0/90 is found to remain close to zero as the applied load increases. The reinforcement of the 90º bundles is certainly a major reason for this negligible transverse deformation, however, the local deformation induced by the release of thermal stresses (Figure12.a) could also have contributed to some extent. On the contrary, the ±45 specimen exhibits quite significant negative values of E_{xx}, which are comparable to those of the axial strain E_{yy}. This might possibly be related to some fibre reorientations under off-axis loading, referred to as “textile effect”, as reported by [29] for SiC/SiC composites. The strain localisations (damage) close to the SiC-Si walls (Figure 8.b and Figure 10.b) might have promoted the reorientations of C_f/C_m blocks. As for the through-thickness strain E_{zz}, values close to zero are observed for the 0/90 specimen at all loading steps, while the ±45 specimen exhibits positive E_{zz} for the late loading increments. This indicates that the delamination is more pronounced under off-axis loading (±45 specimen) than in-axis loading (0/90 specimen), which is confirmed by the principal strain orientations in Figure 11 and Figure 15.

6. Conclusions

In situ tensile XCT tests have been conducted on two C/C-SiC composites, loading relative to different fibre orientations, 0º/90º and ±45º. The 3D microstructures, including wall-like SiC-Si regions, pores and thermal cracks introduced by manufacture have been identified from the XCT images. The local 3D deformations have been probed by DVC and their locations and orientations have been analysed in detail. Two major observations are:

- In both 0/90 and ±45 specimens, significant strain localisations were observed at small applied stress (<50 MPa). The magnitude of the related strains was clearly higher than those induced with higher applied stress. These strain localisations were mostly located inside fibre bundles. They were mainly oriented in the through-thickness direction and represent delamination-like deformation. The origin of these strain localisations is judged to be local tensile residual stresses from processing, which encourage crack initiation on tensile loading and/or pre-existing microcracks that were induced by processing or sample preparation.
- As the axial stress increased, the difference in strain distributions between in-axis (0/90 specimen) and off-axis (±45 specimen) tensile loads became more apparent. At high applied stress, the off-axis tension continued to promote the through-thickness strains (i.e. greater tendency for delamination-like deformation), while the in-axis tension induced more in-plane strains that were affected by the fibre orientations. The high-magnitude strain localisations occur inside the C_f/C_m blocks in the 0/90 specimens and around SiC-Si walls (including the boundaries between +45º and -45º fibre bundles) in the ±45 specimen. This can be rationalised in terms of the interaction between the applied and residual stresses relative to the fibre orientations.

Acknowledgment

The use of facilities funded by EPSRC Grant EP/M02833X/1 “University of Oxford: experimental equipment upgrade” is gratefully acknowledged.

Appendix A. Spherical coordinates and 2D projection coordinates

Figure A.1.as defines the azimuthal angle ϕ and the polar angle θ used in the present study. This choice of ϕ and θ is for facilitating the projection maps of the orientation vectors of principal strains. With this definition, a vector pointing along the Y-axis (the loading axis in the present study) becomes a point within the 2D projection map, whose coordinate system is in Figure A.1.b.

Appendix B: Crack detection by image subtraction technique

A DVC-assisted image subtraction technique [20] has been used to help the detection of the micro-cracks within the composites. It has been performed using the in-house software CMV_3D (Laboratoire Navier). The principal idea of this technique is to first transform the deformed image back into the reference configuration according to the local transformation field evaluated by DVC, then the transformed deformed image is subtracted from the reference image within the reference configuration. The darker voxels in the subtracted images (result of the image subtraction) highlight the newly created cracks. Small regions of the subtracted images are shown in Figure B.1 and Figure B.2 for each specimen at *Load-A* and *Load-AB*, respectively. The same regions are given in the reference image and the transformed deformed image.

In the subtracted images for *Load-A* (Figure B.1), the contrasts are heavily affected by the artefacts, hence no faithful interpretation on the cracks can be drawn. This poor subtraction result is believed to be related to the difference in image quality between the scan of the reference step and the scan at loaded steps.

As for *Load-AB* (Figure B.2), the subtraction results are more convincing and the underlying microstructure is no longer visible after the subtraction procedure. Crack-like features can be detected from the subtracted images by adjusting the greyscale, though their signal is still comparable to that of random noises. Therefore, the interpretation as cracks that is provided hereafter must be considered with caution by the readers. Cracks in the 0/90 specimen seem to have smaller opening than those in the ±45 specimen. In the 0/90 specimen, we focus on the cracks in the transverse bundles (90º bundles). The detected cracks correspond to either the opening of the pre-existing thermal cracks (indicated by crosses of different colours) or the debonding between SiC-Si wall and C_f/C_m block (indicated by the red triangle). In the ±45 specimen, the cracks created by mechanical loading are mostly located beside the SiC-Si walls (see the crosses of different colours), indicating some debonding fracture. This

debonding fracture in both specimens is in agreement with the strain localisations shown in Figure 10, and also provides further arguments for the discussion on Figure 13 in the main text. It is also worth noting that the pre-existing cracks seem not to significantly increase their opening, with an example indicated by the red triangle, which is again consistent with Figure 10 suggesting the lack of systematic correlation between strain localisations and pre-existing cracks.

References

[1] Krenkel W, Berndt F. C/C–SiC composites for space applications and advanced friction systems. Mater Sci Eng A 2005;412:177–81. doi:https://doi.org/10.1016/j.msea.2005.08.204.

[2] Heidenreich B, Manufacture and applications of C/C-SiC and C/SiC composites. Ch. 20 of Processing and Properties of Advanced Ceramics and Composites IV, Volume 234 of Ceramics Transactions, J. P. Singh, N. P. Bansal, T. Goto, J. Lamon, S. R. Choi, M. M. Mahmoud, G. Link eds., ACerS & J. Wiley & sons, NY, pp. 183-198, 2012. doi:10.1002/9781118491867.ch20

[3] Breede F, Hofmann S, Jain N, Jemmali R. Design, manufacture, and characterization of a carbon fiber- reinforced silicon carbide nozzle extension. Int J Appl Ceram Technol 2016;13:3–16. doi:https://doi.org/10.1111/ijac.12496.

[4] Ding W, Shi Y, Kessel F, Koch D, Bauer T. Characterization of corrosion resistance of C / C – SiC composite in molten chloride mixture MgCl 2 / NaCl / KCl at 700 ° C. Npj Mater Degrad 2019;3:1–9. doi:10.1038/s41529-019-0104-3.

[5] Stahl V, Shi Y, Kraft W, Lanz T, Vetter P, Jemmali R, et al. C/C- SiC component for metallic phase change materials. Int J Appl Ceram Technol 2020:1–11. doi:10.1111/ijac.13570.

[6] Hofmann S, Öztürk B, Koch D, Voggenreiter H. Experimental and numerical evaluation of bending and tensile behaviour of carbon-fibre reinforced SiC. Compos Part A Appl Sci Manuf 2012;43:1877–85. doi:https://doi.org/10.1016/j.compositesa.2012.07.017.

[7] Breede F, Koch D, Maillet E, Morscher GN. Modal acoustic emission of damage accumulation in C / C – SiC composites with different fi ber architectures. Ceram Int 2015;41:12087–98. doi:10.1016/j.ceramint.2015.06.026.

[8] Shi Y, Xiu YL, Koch D. Investigation of Statistical Distribution of C/C-SiC Composite's Mechanical Properties. Key Eng. Mater., vol. 809, Trans Tech Publ; 2019, p. 131–9. doi:https://doi.org/10.4028/www.scientific.net/KEM.809.131.

[9] Shi Y, Kessel F, Martin F, Jain N, Tushtev K. Characterization and modeling of tensile properties of continuous fiber reinforced C/C-SiC composite at high temperatures. J Eur

Ceram Soc 2020;41:3061–71. doi:https://doi.org/10.1016/j.jeurceramsoc.2020.09.043.

[10] Kinney JH, Breunig TM, Starr TL, Haupt D, Nichols MC, Stock SR, et al. X-ray tomographic study of chemical vapor infiltration processing of ceramic composites. Science (80-) 1993;260:789–92.

[11] Morales-Rodríguez A, Reynaud P, Fantozzi G, Adrien J, Maire E, Morales-Rodriguez A, et al. Porosity analysis of long-fiber-reinforced ceramic matrix composites using X-ray tomography. Scr Mater 2009;60:388–90. doi:10.1016/j.scriptamat.2008.11.018.

[12] Chateau C, Gélébart L, Bornert M, Crépin J, Boller E, Sauder C, et al. In situ X-ray microtomography characterization of damage in SiCf/SiC minicomposites. Compos Sci Technol 2011;71:916–24. doi:10.1016/j.compscitech.2011.02.008.

[13] Bale HA, Haboub A, Macdowell AA, Nasiatka JR, Parkinson DY, Cox BN, et al. Real-time quantitative imaging of failure events in materials under load at temperatures above 1,600°C. Nat Mater 2013;12:40–6. doi:10.1038/nmat3497.

[14] Chen Y, Gélébart L, Chateau C, Bornert M, King A, Sauder C, et al. Crack initiation and propagation in braided SiC/SiC composite tubes: effect of braiding angle. J Eur Ceram Soc 2020;40:4403–18. doi:https://doi.org/10.1016/j.jeurceramsoc.2020.04.060.

[15] Wang L, Zhang W, Li H, Hou C, Ren F. 3D in-situ characterizations of damage evolution in C/SiC composite under monotonic tensile loading by using X-ray computed tomography. Appl Compos Mater 2020;27:119–30. doi:https://doi.org/10.1007/s10443-020-09796-5.

[16] Buljac A, Jailin C, Mendoza A, Neggers J, Taillandier-Thomas, T., Bouterf A, Smaniotto B, et al. Digital volume correlation: review of progress and challenges. Exp Mech 2018;58:661–708. doi:https://doi.org/10.1007/s11340-018-0390-7.

[17] Saucedo-Mora L, Lowe T, Zhao S, Lee PD, Mummery PM, Marrow TJ. In situ observation of mechanical damage within a SiC-SiC ceramic matrix composite. J Nucl Mater 2016;481:13–23. doi:10.1016/j.jnucmat.2016.09.007.

[18] Mazars V, Caty O, Couégnat G, Bouterf A, Roux S, Denneulin S, et al. Damage investigation and modeling of 3D woven ceramic matrix composites from X-ray tomography in-situ tensile

tests. Acta Mater 2017;140:130–9. doi:10.1016/j.actamat.2017.08.034.

[19] Wan F, Liu R, Wang Y, Cao Y, Zhang C, Marrow TJ. Damage development during flexural loading of a 5-directional braided C/C-SiC composite, characterized by X-ray tomography and digital volume correlation. Ceram Int 2019;45:5601–12. doi:https://doi.org/10.1016/j.ceramint.2018.12.020.

[20] Chateau C, Nguyen TT, Bornert M, Yvonnet J. DVC-based image subtraction to detect microcracking in lightweight concrete. Strain 2018;e12276. doi:https://doi.org/10.1111/str.12276.

[21] Chen Y, Gélébart L, Chateau C, Bornert M, King A, Aimedieu P, et al. 3D detection and quantitative characterization of cracks in a ceramic matrix composite tube using X-ray computed tomography. Exp Mech 2020;60:409–24. doi:10.1007/s11340-019-00557-5.

[22] British-Standards-Institute-Staff. Advanced Technical Ceramics. Ceramic Composites. Physical Properties. Determination of Density and Apparent Porosity. B S I Standards; 2004.

[23] Straumit I, Lomov S V., Wevers M. Quantification of the internal structure and automatic generation of voxel models of textile composites from X-ray computed tomography data. Compos Part A Appl Sci Manuf 2015;69:150–8. doi:10.1016/j.compositesa.2014.11.016.

[24] Sha J, Wang S, Dai J, Zu Y, Li W, Sha R. High-temperature Mechanical Properties and Their Influence Mechanisms of ZrC-Modified C-SiC Ceramic Matrix Composites up to 1600 ◦ C 2020. doi:https://doi.org/10.3390/ma13071581.

[25] Marques FC, Lacerda RG, Champi A, Stolojan V, Cox DC, Silva SRP. Thermal expansion coefficient of hydrogenated amorphous carbon. Appl Phys Lett 2003;83:3099–101. doi:https://doi.org/10.1063/1.1619557.

[26] Breede F, Koch D, Maillet E, Morscher GN. Modal acoustic emission of damage accumulation in C/C–SiC composites with different fiber architectures. Ceram Int 2015;41:12087–98. doi:https://doi.org/10.1016/j.ceramint.2015.06.026.

[27] Nozawa T, Katoh Y, Kohyama A. Evaluation of Tensile Properties of SiC/SiC Composites with Miniaturized Specimens. Mater Trans 2005;46:543–51.

doi:https://doi.org/10.2320/matertrans.46.543.

[28] Bernachy-Barbe F, Gélébart L, Bornert M, Crépin J, Sauder C. Anisotropic damage behavior of SiC/SiC composite tubes: Multiaxial testing and damage characterization. Compos Part A Appl Sci Manuf 2015;76:281–8. doi:10.1016/j.compositesa.2015.04.022.

[29] Bernachy-Barbe F, Gélébart L, Bornert M, Crépin J, Sauder C. Characterization of SiC/SiC composites damage mechanisms using Digital Image Correlation at the tow scale. Compos Part A Appl Sci Manuf 2015;68:101–9. doi:10.1016/j.compositesa.2014.09.021.

Figures

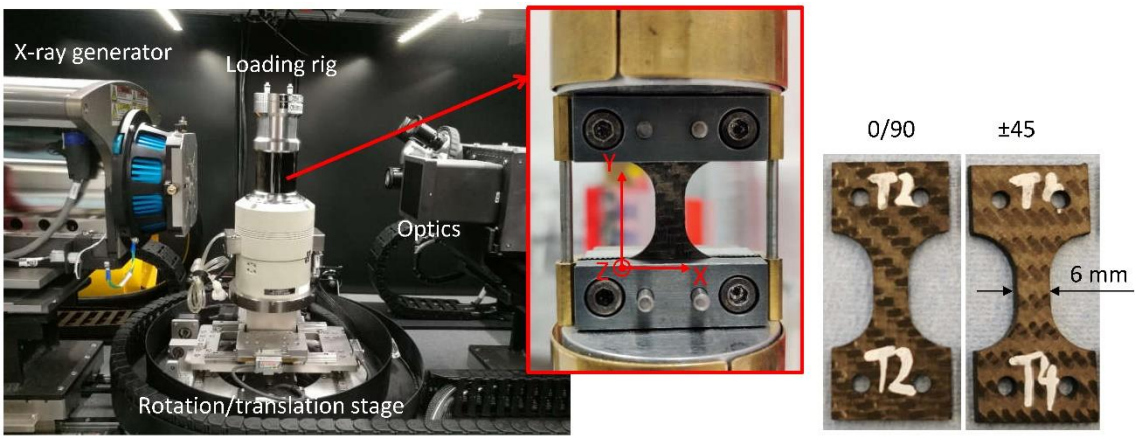

Figure 1: Experimental setup for the in-situ tensile tests with the two tested specimens shown on the right.

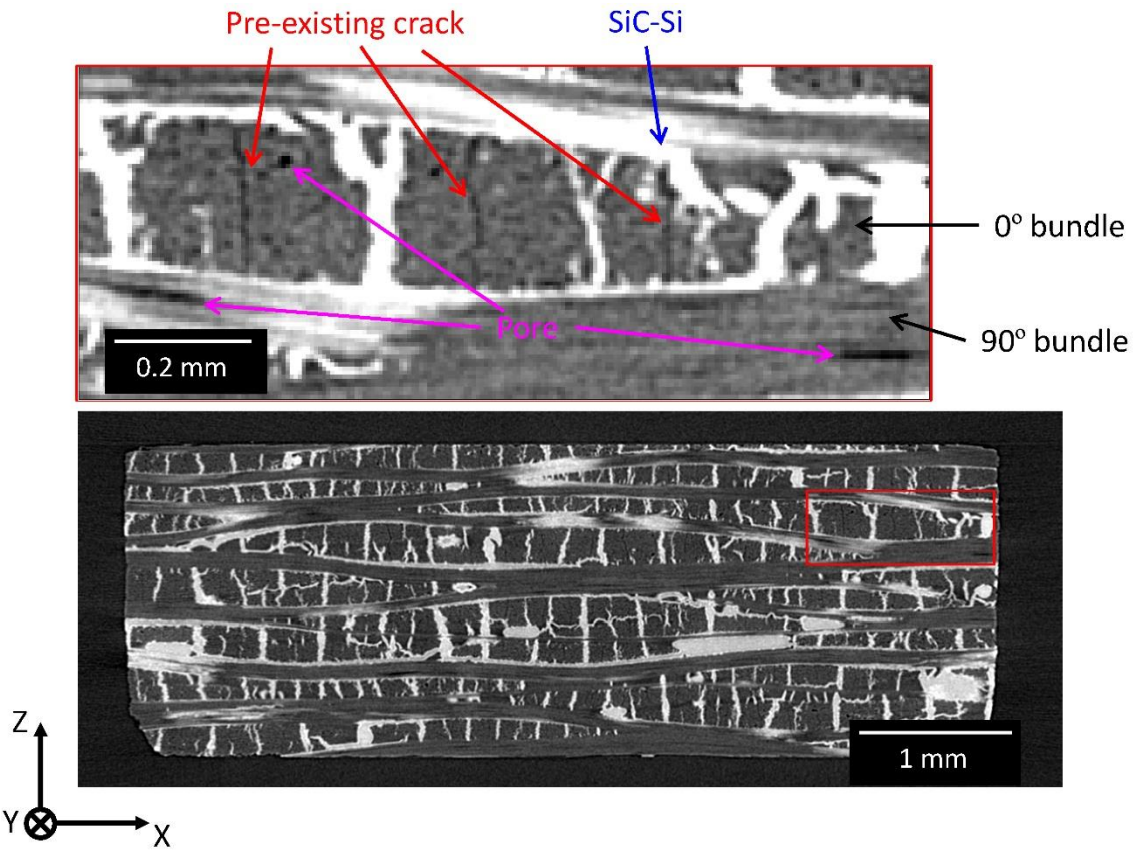

Figure 2: A cross-sectional slice (XZ plane) and its zoom-in of the reconstructed XCT image of the 0/90 specimen at reference state (unloaded). The tension direction is along the Y-axis. The greyscale of the zoomed-in view has been adjusted to make the darker pores and cracks more visible.

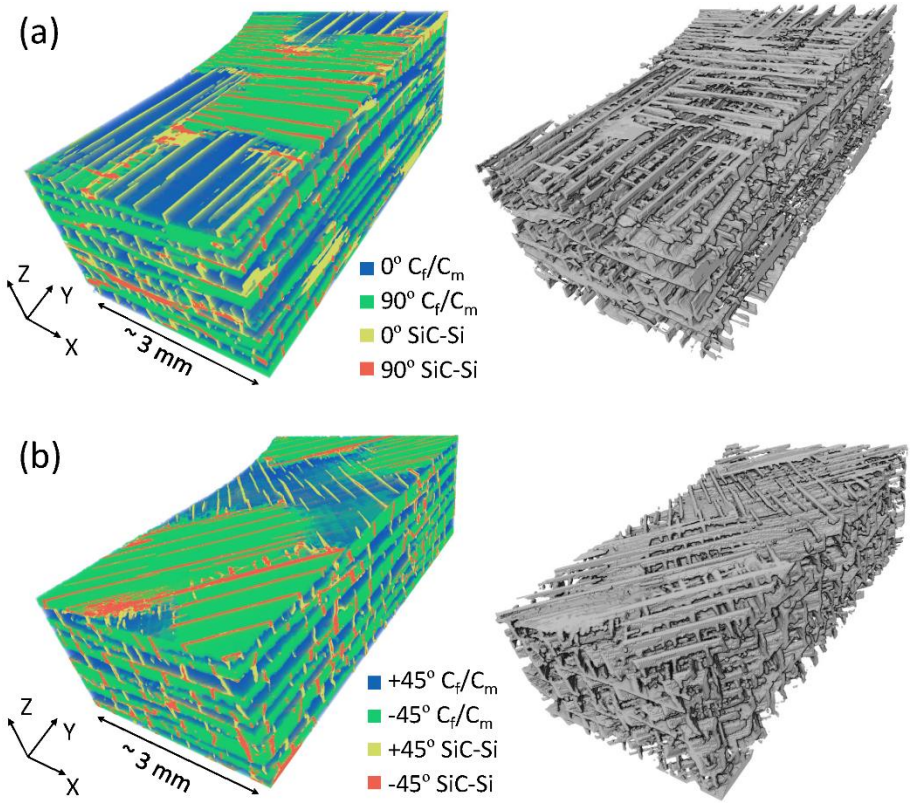

Figure 3: Image segmentation results for (a) the 0/90 specimen and (b) the ±45 specimen. Only a quarter of the specimen is shown for the sake of visibility. The left images show all identified phases, and the right images show the wall-like structure of SiC-Si.

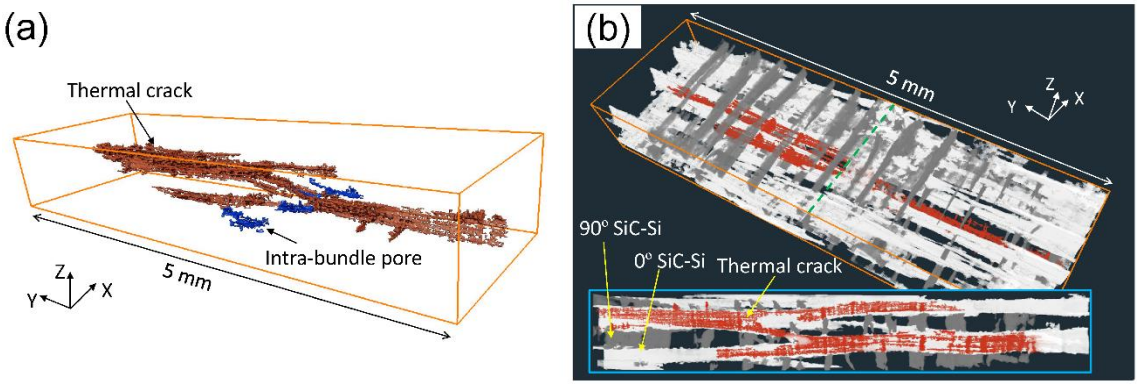

Figure 4: 3D visualisation of example intra-bundle pores (blue) and thermal crack (red): (a) pores and crack only; (b) the thermal crack with surrounding SiC-Si of different orientations (labelled as grey and white).

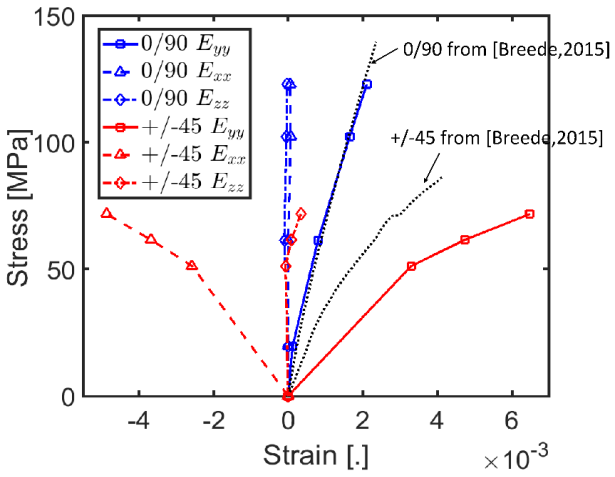

Figure 5: Macroscopic strains versus macroscopic stresses at each loading step of the 0/90 and ±45 specimens. The black dotted curves show the measurements from continuous tests of [26] on similar composites yet with much larger specimen dimensions (60 × 10 × 3 mm in the length, width and thickness directions of the gauge section).

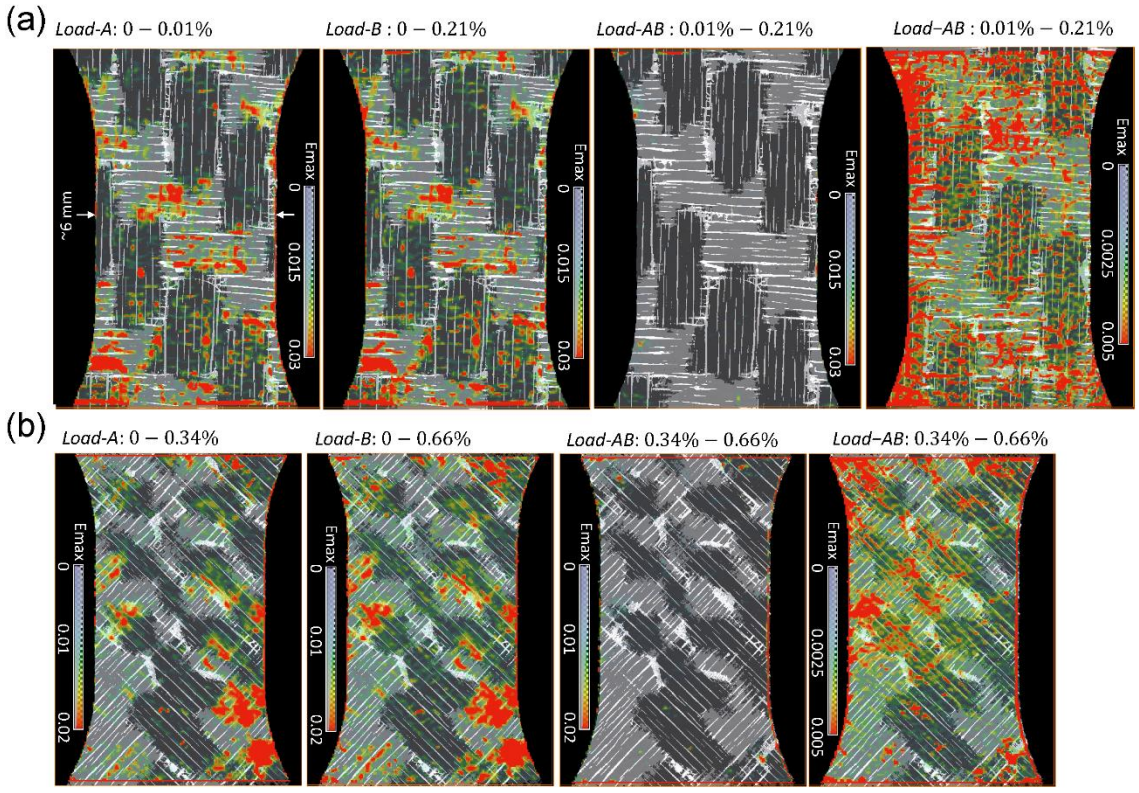

Figure 6. Distributions of the maximum principal strains ε_{max} in the XY plane for different loading increments of (a) the 0/90 specimen and (b) the ±45 specimen. At the rightest side of each graph shows

the strains for *Load-AB* with a tighter range of the colour bar to increase the visibility of the strain patterns.

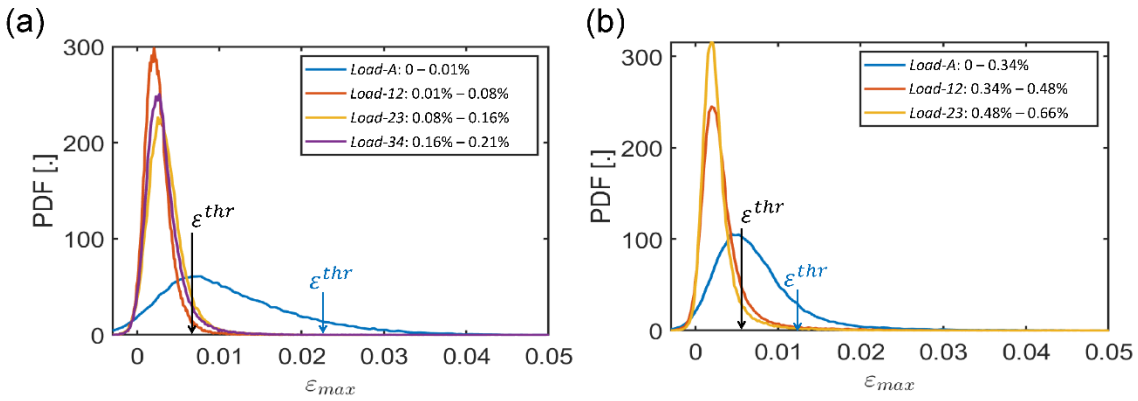

Figure 7. Probability density functions of the maximum principal strains ε_{max} measured between each two sequential loading steps *Load-ij* for (a) the 0/90 specimen and (b) the ±45 specimen. The arrows indicate the threshold values ε^{thr} separating the high-magnitude strains and low-magnitude strains.

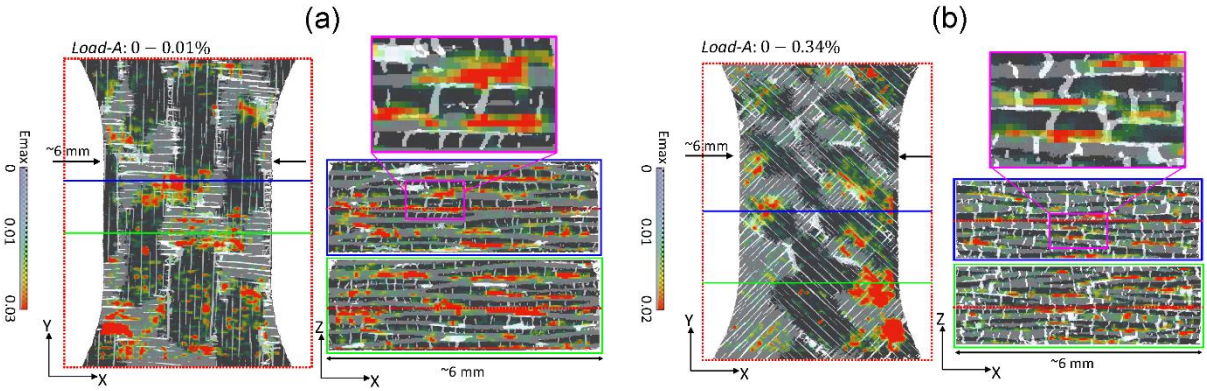

Figure 8. Location of high-magnitude strains ($\varepsilon_{max} > \varepsilon^{thr}$) induced by *Load-A* in (a) the 0/90 specimen and (b) the ±45 specimen.

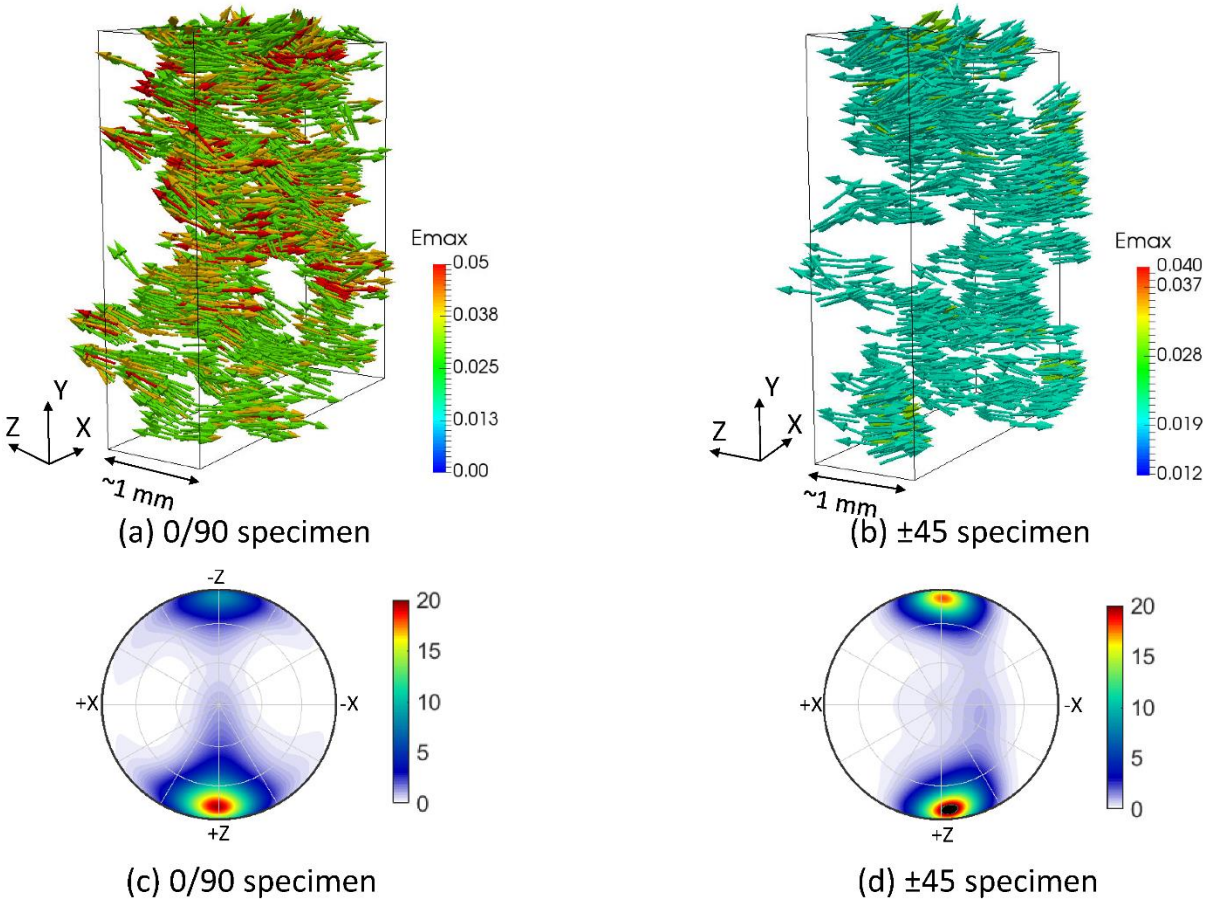

Figure 9. Principal orientations of the high-magnitude strains ($\varepsilon_{max} > \varepsilon^{thr}$) induced by *Load-A* in the two specimens. (a,b) 3D visualisation of the principal eigenvectors of strains in a subvolume in the middle of each specimen. For the sake of visibility, only one out of three vectors is shown. (c,d) Densities of the principal eigenvector orientations, displayed in stereographic projection (see Appendix A for the definition).

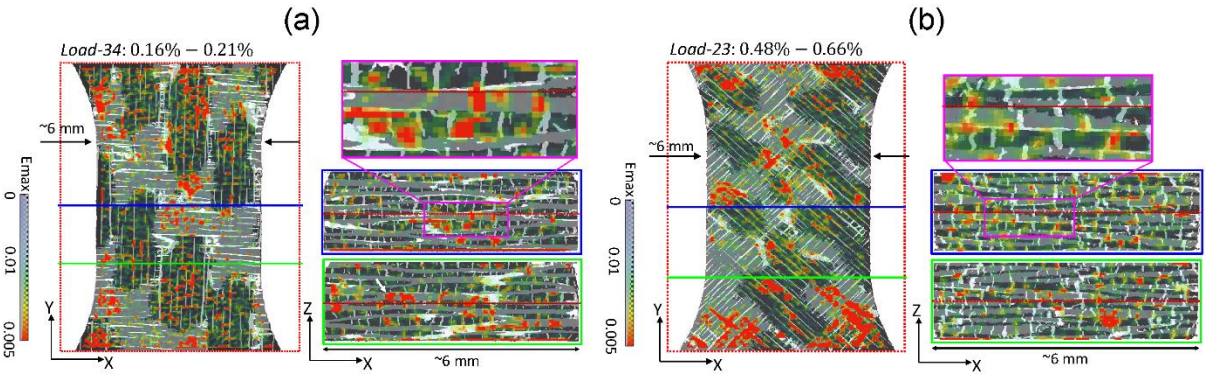

Figure 10. Locations of high-magnitude strains ($\varepsilon_{max} > \varepsilon^{thr}$) induced by the last loading increment in (a) the 0/90 specimen and (b) the ±45 specimen.

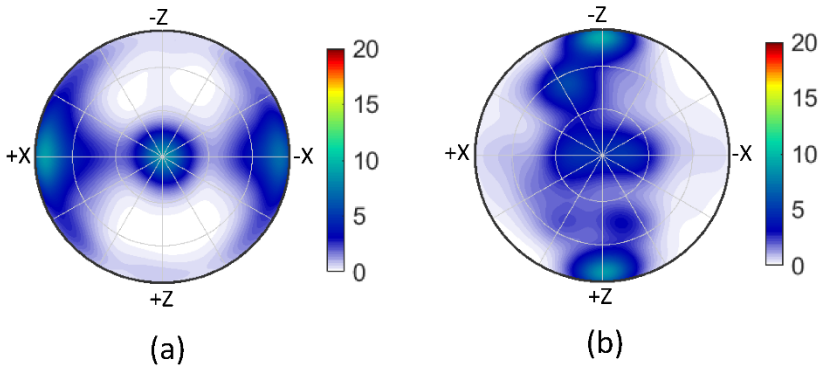

Figure 11. Densities of the principal orientations of the high-magnitude strains ($\varepsilon_{max} > \varepsilon^{thr}$) created by the last loading increment *Load-34* for the 0/90 specimen (a) and *Load-23* for the +/-45 specimen (b).

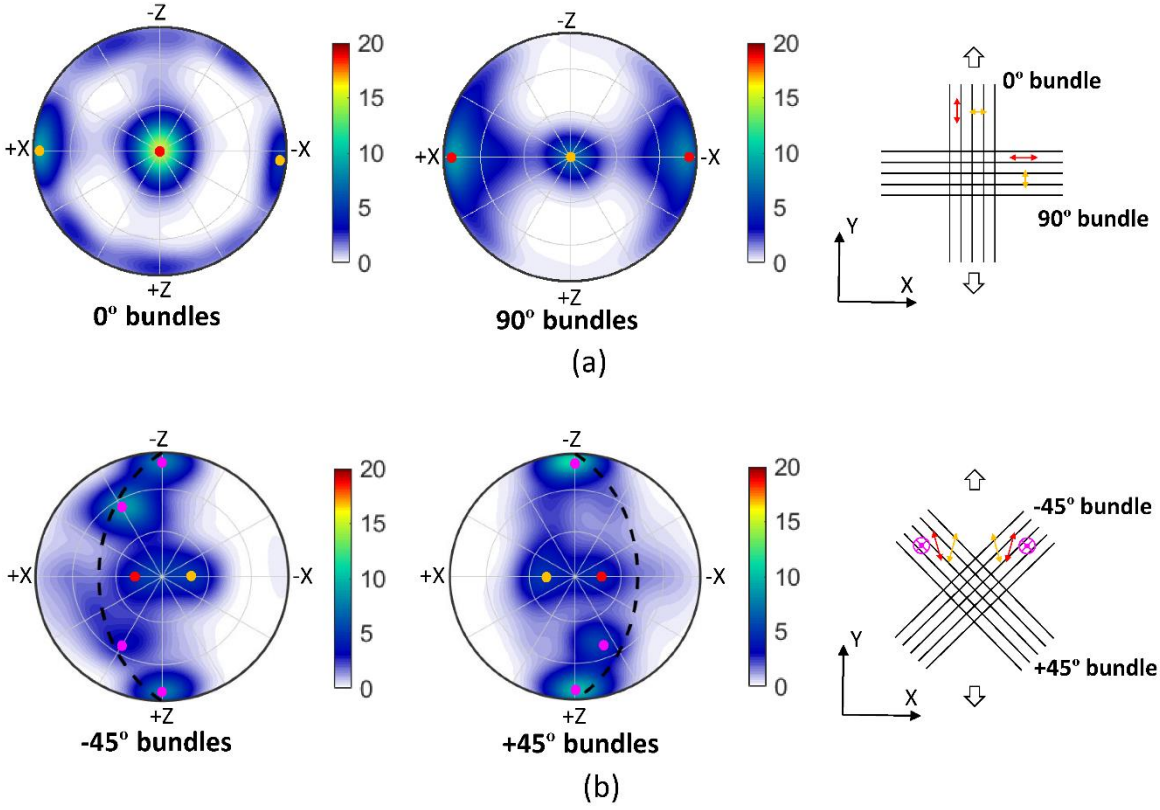

Figure 12. Densities of the principal orientations of the high-magnitude strains ($\varepsilon_{max} > \varepsilon^{thr}$) at the last loading increment, measured within the fibre bundles with different orientations of each specimen. The dashed lines in (b) mark the great circles corresponding to the YZ plane rotated around the Z-axis by -45º and +45º (left and right, respectively). Schematics on the right of each graph illustrate the principal strain orientations (red arrows) in each type of fibre bundles deduced from the densities of orientations, with the coloured arrows corresponding to the coloured dots in the stereographic maps.

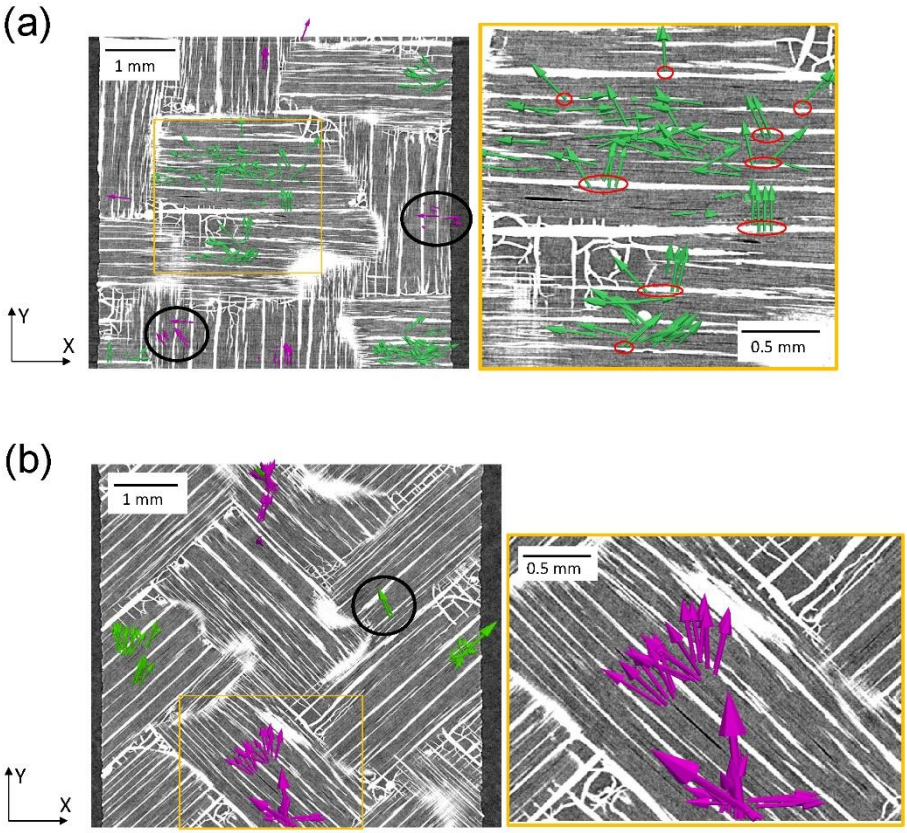

Figure 13. Principal vectors of the high-magnitude strains ($\varepsilon_{max} > \varepsilon^{thr}$) created at the last loading increment of (a) the 0/90 specimen and (b) the ±45 specimen. The vectors are shown in 3D, while the woven structure is shown through a 2D slice of the XCT image located at the strains under investigation. The vectors in the bundles of different orientations are distinguished by two different colours. The starting point of arrow is the position at which the strain is measured.

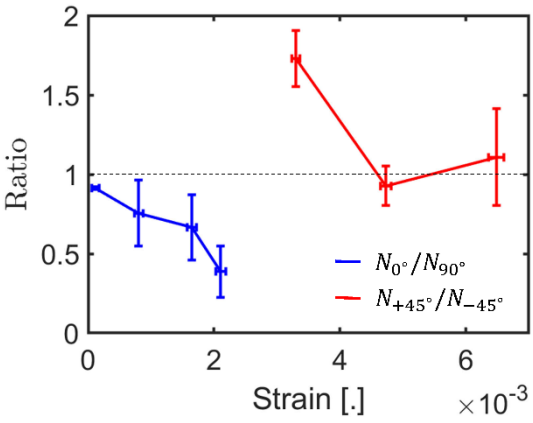

Figure 14. Ratio of number of high-magnitude strain points between the two groups of fibre bundles with different orientations in each specimen.

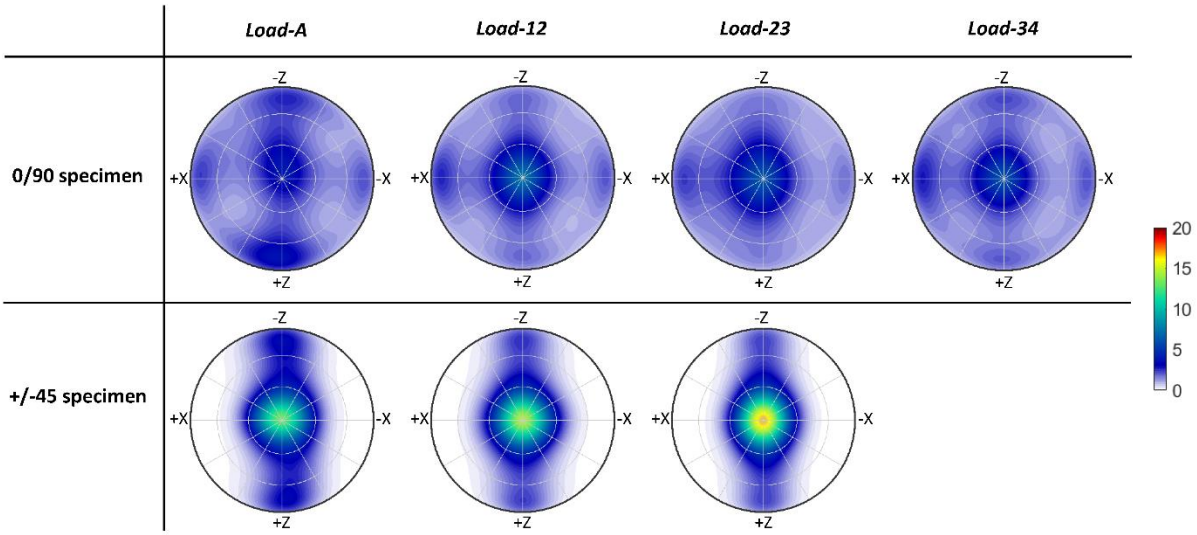

Figure 15. Densities of principal orientations of low-magnitude strains ($\varepsilon_{max} < \varepsilon^{thL}$) for the two specimens at different loading increments.

Tables

Specimen	Step1 (MPa)	Step2 (MPa)	Step3 (MPa)	Step4 (MPa)
0/90	20 ±0.1	61 ±0.2	102 ±0.3	123 ±0.4
±45	51 ±0.1	62 ±0.2	72 ±0.2	-

Table 1. Tensile stresses for each step of the two specimens. Stresses were calculated by the ratio between the measured force and the cross-section area of dog-bone specimen.

Notation	*Load-A*	*Load-B*	*Load-AB*	*Load-12*	*Load-23*	*Load-34*
0/90	Ref. – Step1	Ref. – Step4	Step1 – Step4	Step1 – Step2	Step2 – Step3	Step3 – Step4
±45	Ref. – Step1	Ref. – Step3	Step1 – Step3	Step1 – Step2	Step2 – Step3	-

Table 2. Summary of the loading steps between which the DVC calculations were conducted in the present work. The final loading step is Step4 is for the 0/90 specimen and Step3 for the ±45 specimen.

Appendix

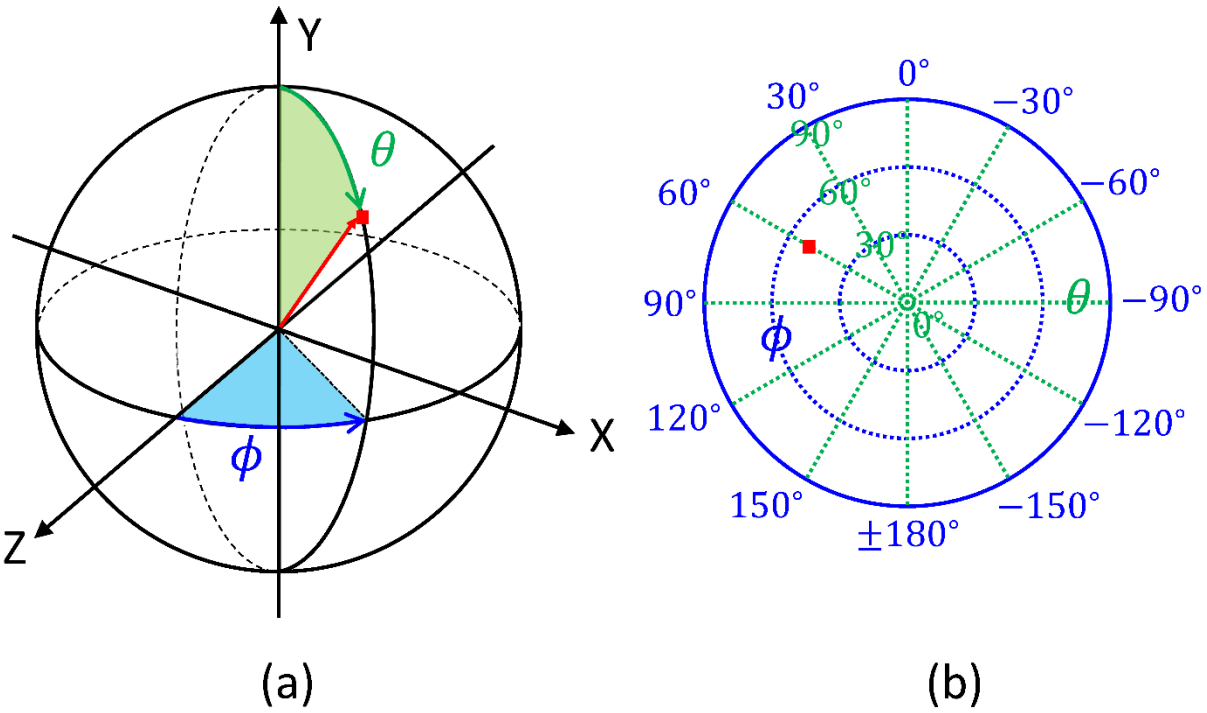

Figure A.1. (a) Definition of the azimuthal angle ϕ and the polar angle θ of the spherical coordinate system used in the present work. (b) The 2D projection coordinate systems expressed by the azimuthal and polar angles. The red point is shown in both the 3D spherical and the 2D projection coordinates to give an example.

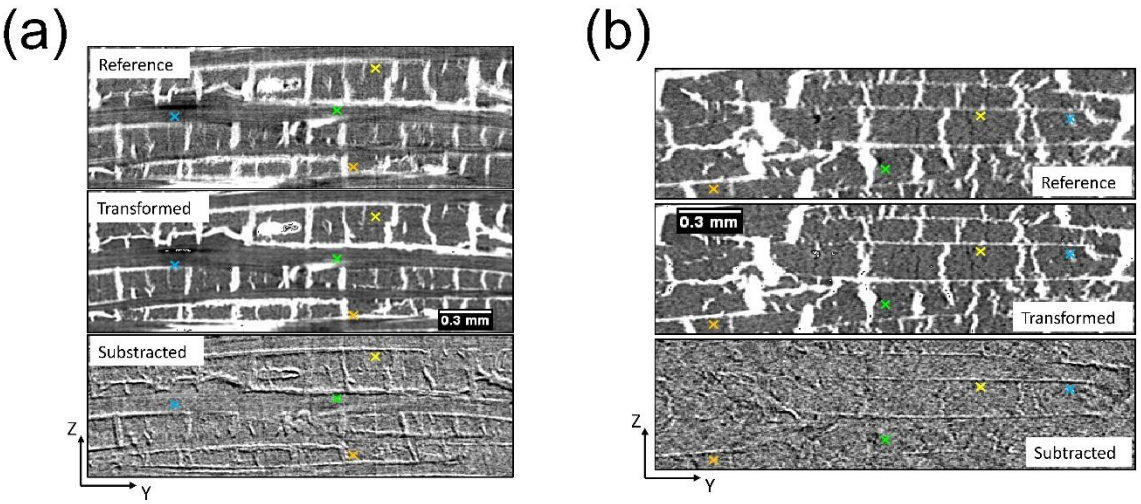

Figure B.1. Image subtraction at Load-A for (a) the 0/90 specimen and (b) the ±45 specimen. The crosses of different colours are used to highlight the same position within different images. The greyscales of each image has been adjusted to make microstructural features more visible.

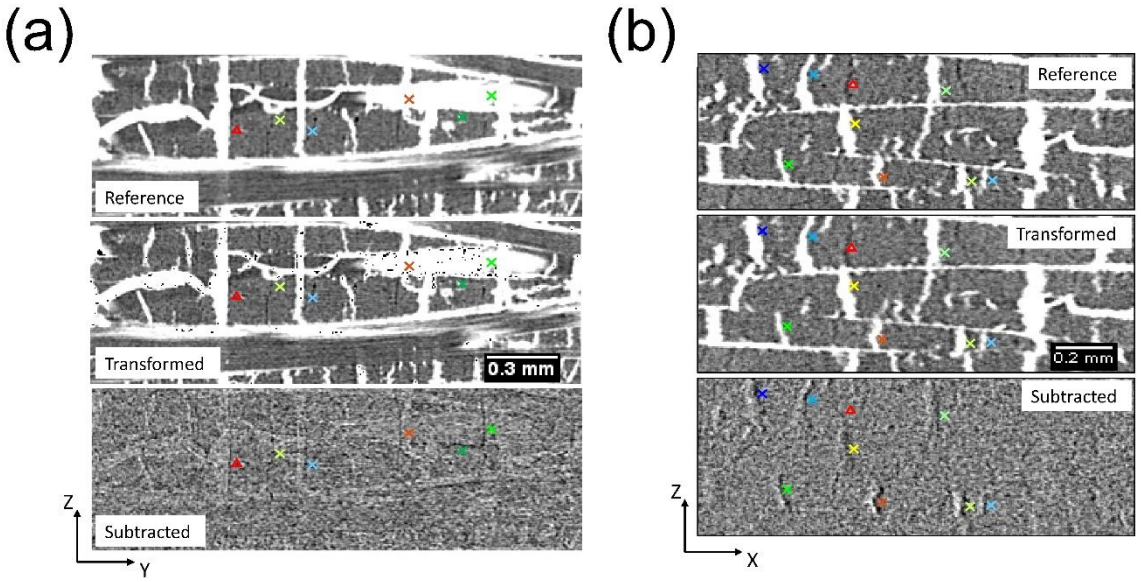

Figure B.2. Image subtraction results at *Load-AB* for (a) the 0/90 specimen and (b) the ±45 specimen. The crosses and the triangle of different colours are used to highlight the same position within different images. The greyscales of each image has been adjusted to make microstructural features more visible.

Supplementary Materials

Supplementary material 1

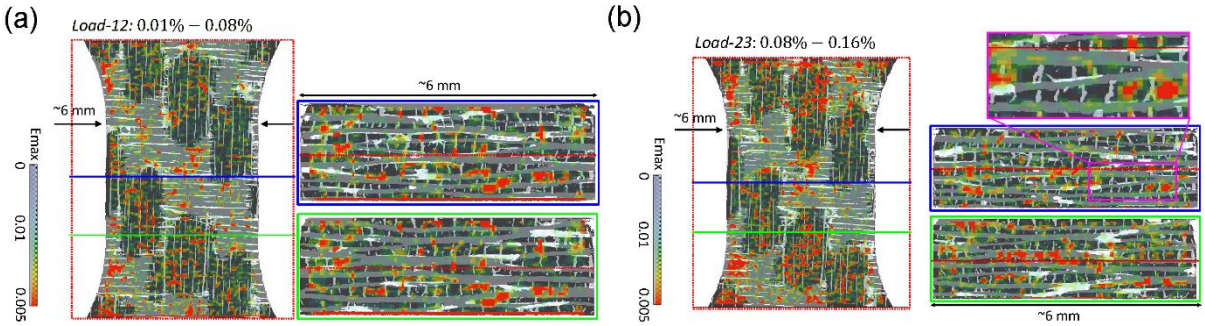

Figure S1. Locations of high-magnitude strains ($\varepsilon_{max} > \varepsilon^{thr}$) induced by the intermediate loading increment in the 0/90 specimen.

Supplementary material 2

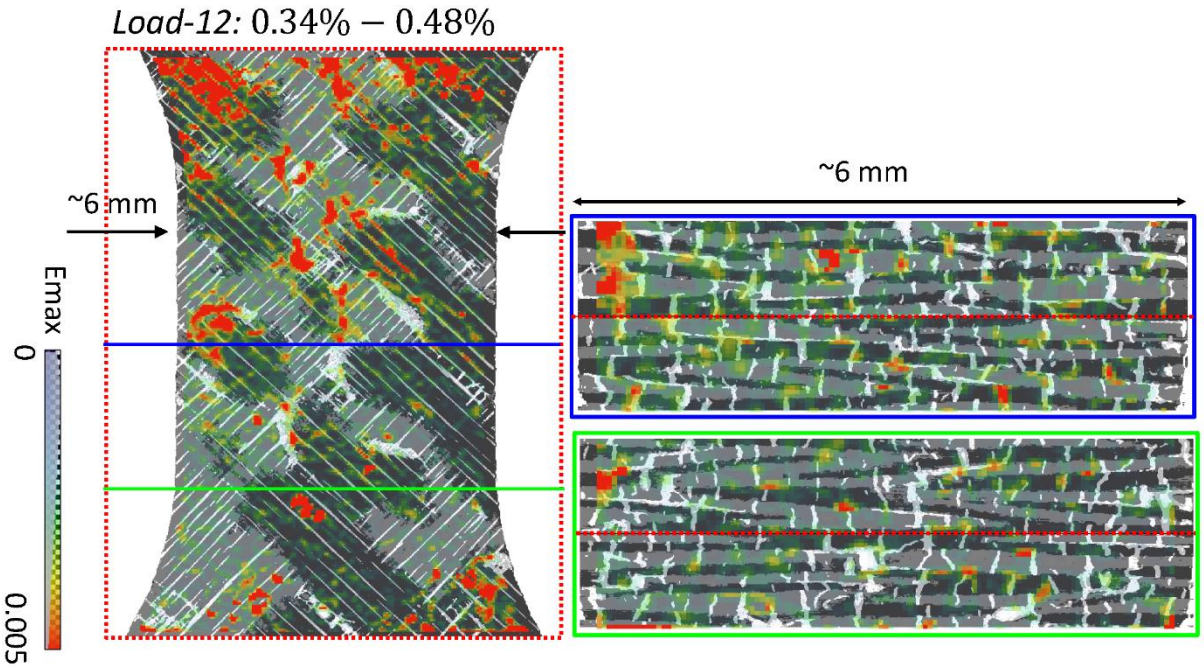

Figure S2. Locations of high-magnitude strains ($\varepsilon_{max} > \varepsilon^{thr}$) induced by the intermediate loading increment in the 0/90 specimen.

Supplementary material 3

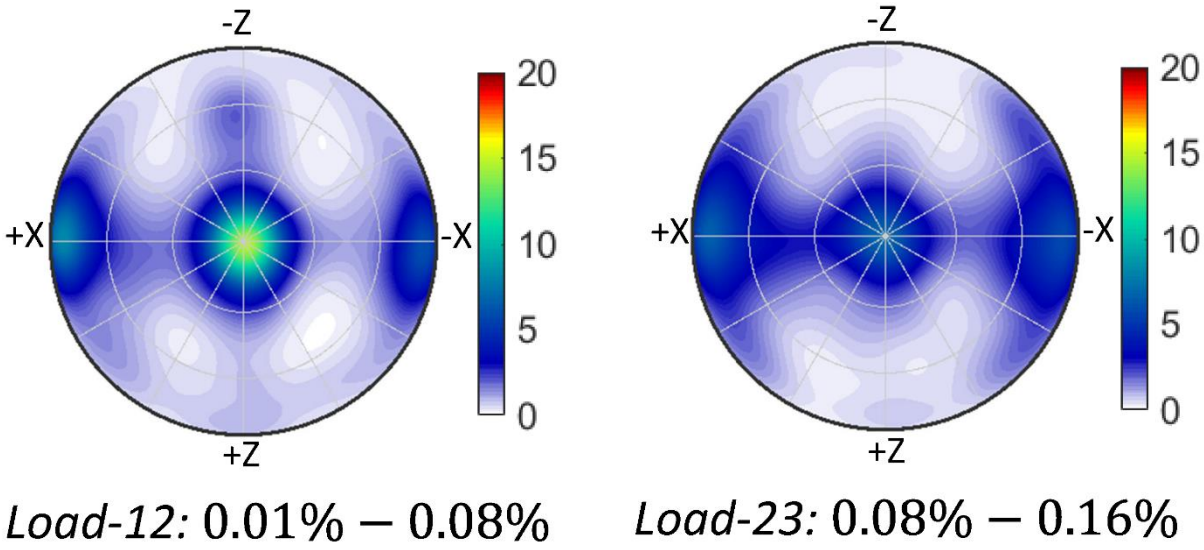

Figure S3. Densities of the principal orientations of the high-magnitude strains ($\varepsilon_{max} > \varepsilon^{thr}$) created by the intermediate loading increments *Load-12* and *Load-23* for the 0/90 specimen.

Supplementary material 4

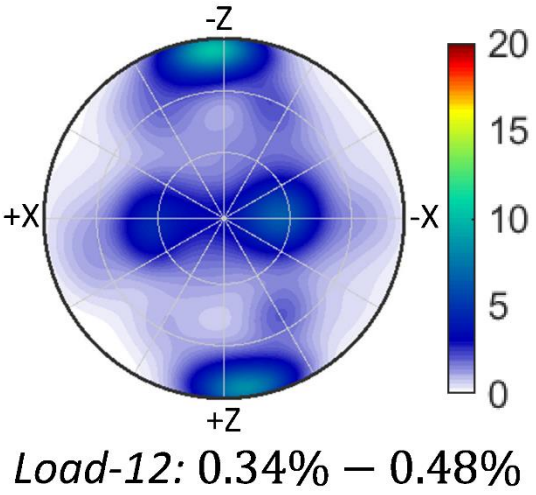

Figure S4. Densities of the principal orientations of the high-magnitude strains ($\varepsilon_{max} > \varepsilon^{thr}$) created by the intermediate loading increment *Load-12* for the +/-45 specimen.

Supplementary material 5

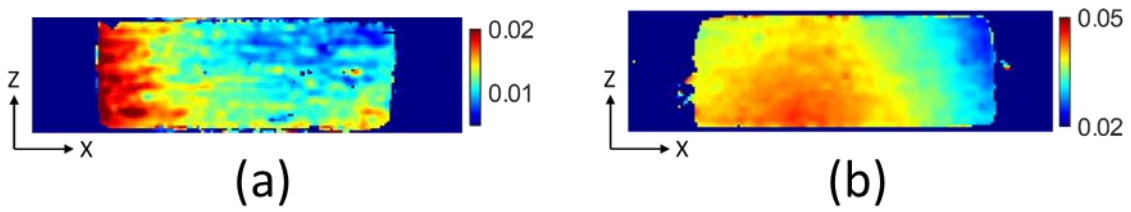

Figure S5. Maps of relative Y-axis displacements (loading direction) between the upper and lower cross sections of the centre gauge region (a) for the 0/90 specimen and (b) for the ±45 specimen. Both graphs show the results comparing the reference and the last loading step. The colour bar is in millimetre.

Specimen	E_{XX}	E_{YY}	E_{ZZ}	E_{XY}	E_{XZ}	E_{YZ}
0/90	-4.8e-03	6.4e-03	4.4e-04	1.2e-04	-6.0e-05	1.9e-04
±45	4.7e-05	2.1e-03	9.8e-06	3.4e-04	-5.9e-05	2.2e-04

Table S5. Macroscopic strain components of the central gauge region of each specimen accommodated between the reference step and the last loading step.

Figure S5 shows the difference of Y-axis displacement (measured from DVC) between the upper and the lower cross sections of the gauge region of the 0/90 specimen and the macroscopic deformation is slightly higher on the left than on the right of the specimen, suggesting a slight misalignment might exist despite the precautions taken. Moreover, the macroscopic strain tensor of the central gauge region of each specimen is calculated using the DVC-measured displacements and given in Table S5. Although the shear components are not negligible to the principal strain in the loading direction (E_{YY}), they are only 1/10 of the loading strain E_{YY}. Therefore, the slight misalignment should not affect the discussions presented in the main text, as the major loading mode is still tension.